ADVANCED ENGINEERING MATERIALS
www.aem-journal.com

A Time-Saving Method for Evaluating the Fatigue Strength of Carburized High-Alloy Steel Containing Carbides

Zikuan Xu, Xuezhong Gu, Xiaolong Liu, Weihao Chen, Bin Wang, Peng Zhang,* Maosheng Yang, Hongxiao Chi, and Zhefeng Zhang**

To propose a time-saving method for evaluating the fatigue strength of carburized steel, the fatigue behavior and fracture mechanism of carburized 14Cr14Co13Mo5 steels are studied by the rotary bending fatigue tests. It is found that the fatigue crack initiation site changes from surface to internal after carburizing due to the residual compressive stress and carbide cluster caused by the carburization. Besides, a notable correlation between the stress intensity of the cracked carbides at fatigue crack initiation site and fatigue life is observed in the carburized samples. This correlation allows for the estimation of fatigue strength at long conditional life based on samples tested at relatively high stress amplitudes with short lives, achieving a prediction error within 10% for the material studied. A significant time saving of ≈65% compared to the staircase method is achieved. The proposed method has significant implications for improving the efficiency fatigue strength evaluation in carburized steels containing carbides.

1. Introduction

Many industrial components, such as gears and bearings in transmission systems and engines, have a serious risk of fatigue failure. Therefore, the surface-hardening treatment technology has been widely applied to improve the fatigue performance of these machine components, such as the carburizing treatment.[1–5] Assessing the effectiveness of carburizing processes typically requires numerous fatigue tests, which are both costly and time-consuming. Therefore, developing a method to rapidly predict and evaluate the fatigue performance of carburized steel is of great importance for optimizing the carburizing process.

In recent years, time-saving evaluation methods have advanced rapidly and can be broadly classified into two categories. One involves the development of new detection equipment that focuses on parameters such as temperature[6] and stiffness.[7] However, this type of detection is primarily applicable to uniaxial tension fatigue tests, enabling direct examination of fatigue samples. For loading methods like rotary bending, where samples are continuously rotating, the implementation of such detection becomes challenging. Additionally, another category involves evaluation method based on the probability and statistics theory of fatigue tests.[8] As reported, the testing period could be 1/5–1/3 of that by the common up-and-down method for 16 samples.[8] Nevertheless, the time savings are achieved by testing multiple samples simultaneously, meaning that the overall number of samples and the associated testing costs have not been diminished.

Attempts have also been made to establish relationships between indicators based on static properties and fatigue performance for predictive purposes. The effective case depth is commonly used as an indicator of the state of samples produced by various carburizing treatments.[9–12] Numerous studies have been conducted on the relationship between effective case depth and bending fatigue strength in carburized steels in order to rapidly assess the fatigue performance. Xiao et al.[12] summarized the fatigue data from the available literature and found that the fatigue strength of carburized steels generally increased initially and then decreased as the effective case depth increased. However, the effective case depth alone cannot fully capture the effects of carburizing treatment because there are many factors affecting the fatigue properties of carburized steels, mainly including the distribution of residual compressive stress and the presence of globular and network carbide.[12–14] The effective case depth, which ignores these influencing factors on fatigue life, can only be used as an empirical parameter, resulting in unacceptable prediction accuracy.

In the last few years, some researchers carried out the fatigue properties prediction of the laboratory samples containing residual stress and hardness gradient of carburized bearing steels. Genel[10] proposed simple expressions for the case-hardened

Z. Xu, X. Gu, X. Liu, W. Chen, B. Wang, P. Zhang, Z. Zhang
Shenyang National Laboratory for Materials Science
Institute of Metal Research
Chinese Academy of Sciences
Shenyang 110016, China
E-mail: bwang12s@imr.ac.cn; pengzhang@imr.ac.cn; zhfzhang@imr.ac.cn

X. Liu
School of Mechanical Engineering
Liaoning Shihua University
Fushun 113001, China

M. Yang, H. Chi
Institute for Special Steels
Central Iron & Steel Research Institute
Beijing 100081, China

The ORCID identification number(s) for the author(s) of this article can be found under https://doi.org/10.1002/adem.202402041.

DOI: 10.1002/adem.202402041

steels to estimate the bending fatigue strength and optimum effective case depth values. Savaria et al.[15] proposed a 3D fatigue model taking into account residual stresses, hardness gradient, and surface roughness for the prediction of the bending fatigue strength. However, the method based on the influence of carbides upon fatigue performance of the carburized steels is rare. Nevertheless, high-temperature bearing steels like CSS42L and 14Cr14Co13Mo5, which are developed to endure higher operating temperatures, commonly form carbides after the carburization process.

Recently, Yin et al.[16] Tian et al.[17] and He et al.[18] carried out detailed investigation on the effects of carburizing treatment on the microstructure of the case layer in high-alloy steel. The result of a 14Cr14Co13Mo4 martensitic stainless steel showed that the second phase was mainly composed of $M_{23}C_6$ and M_6C.[16] In addition, the coarse carbides would appear at the grain boundaries of the prior austenite.[17] For the fatigue performance, Guo et al.[19] found that the fatigue cracks of M50 bearing steel primarily nucleated through the primary carbide under cyclic loading. Schmid et al.[20] also had reported that the fatigue failure occurred at primary chromium carbides in a martensitic stainless 18% chromium steel. Sohar et al.[21] reported that the primary carbides and carbide clusters turned out to be the fatigue crack origins.

However, although the influence of carbides is noteworthy, the fatigue strength prediction model that fully considers the influence of carbides has not yet been seen. In related researches, Xue et al.[22] reported the application of the Murakami method[23] for predicting fatigue strength associated with carbide cracking. However, it is noteworthy that this method does not account for the potential influence of conditional lifetime on fatigue strength. A potential approach to rapidly evaluating the fatigue strength of this carburized bearing steel involves establishing a relationship between fatigue lifetime and the fatigue damage parameters, such as the stress intensity factor (SIF) of carbide, allowing for the prediction of long-life fatigue strength based on short-life data.

In the present work, the fatigue behavior of carburized 14Cr14Co13Mo5 steel under rotating bending load was investigated. The aim of the current study is to propose a fast evaluation method for fatigue strength prediction of carburized steel based on the effects of carbide on the fatigue performance. Meanwhile, the microstructure, residual compressive stress, and fatigue failure mechanism are also analyzed.

2. Experimental Section

The material used in the present study was a 14Cr14Co13Mo5 martensitic stainless steel whose chemical composition (wt%) could be seen in **Table 1**. The as-received material was represented by S0.

Table 1. Elemental compositions of the present material before carburizing (wt%).

C	Cr	Mo	Co	Ni	V	W	Mn	Si	Fe
0.16	13.91	4.68	13.5	1.99	0.58	0.60	≤0.05	0.075	Bal.

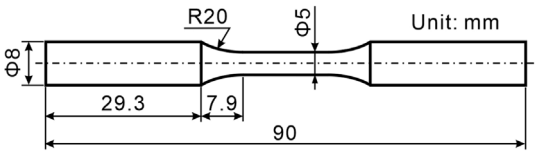

Figure 1. Schematic diagram of the fatigue sample.

The semifinished fatigue samples with a reduced section of 5.6 mm diameter were machined and then mechanically polished by sandpaper. Subsequently, the low-pressure gas carburization was performed with carbon potential in the range of 0.8–1.2%, of which the detailed process could be seen in ref. [16]. In order to produce material with different effective case depths, four different treatment times were employed, represented by S1, S2, S3, and S4, respectively, where the carburizing duration progressively increased from S1 to S4. After carburizing heat treatment, it was quenched with oil from 1100 °C. The subsequent cryogenic treatment process below −85 °C promoted the martensitic transformation followed by a tempering treatment at 520 °C. Finally, 0.3 mm was removed from the sample surface by mechanical processing followed by mechanical polishing treatment obtaining a mirror finish. The final size configuration of the fatigue sample could be seen in **Figure 1**.

The microhardness was measured using a LECO AMH43 automatic microhardness tester fitted with a Vickers indenter. The load was 500 g, and the dwell time was 12 s. One sample and three sets of points were tested for each group and half of the difference between the maximum and minimum hardness was used as the error bar for every depth. The distance between adjacent points is 100 μm, distributed along the radius of sample. Each set consists of 25 points. Residual stress testing was conducted by PROTO LXRD in accordance with the ASTM-E915-2010 standard. The phase composition was characterized by OXFORD SYMMETRY S2 electron backscattered diffraction (EBSD) and the elemental distribution was analyzed by the OXFORD ULTIM MAX 40 energy-dispersive spectroscopy (EDS) on ZEISS SIGMA 500 scanning electron microscope (SEM). For EBSD, the step size was set to 100 nm and four phases, Iron FCC, Iron BCC, Fe_3Mo_3C, and $Cr_{18.93}Fe_{4.07}C_6$, were detected. The EDS and EBSD on SEM were employed to qualitatively analyze the types of carbides. The samples of microstructure, residual stress, and microhardness tests were cut from the fatigue samples that had not undergone fatigue testing.

The fatigue performances were carried out on a rotary bending fatigue testing machine with a load ratio (ratio of minimum to maximum stress) of $R = -1$ at a frequency of 50 Hz based on the standard ISO 12 107:2003. The fracture morphologies of fatigue samples were observed by SEM, and the carbides in the fatigue crack initiation region were analyzed by the EDS on SEM.

3. Results and Discussion

3.1. Microhardness, Microstructure, and Residual Stress

Carburizing treatment has complex effects on the changes in microstructure and properties such as hardness and residual

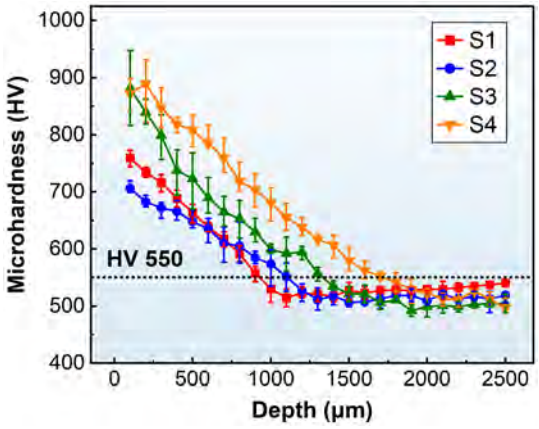

Figure 2. Microhardness distribution profiles of the carburized steels across S1–S4 groups.

stress, making it difficult to evaluate the heat treatment process based on a single factor. Among the various factors that affect the fatigue performance of carburized steel, effective case depth is a widely used parameter.[3,11] According to the ISO 18 203:2016 standard, the part with a microhardness greater than 550 HV is defined as the effective case depth. The microhardness distributions of the four groups of samples with different characteristics are shown in **Figure 2**. The hardness gradually decreases from the surface to the core in general, as shown in Figure 2. According to the hardness test results in Figure 2, the effective case depth is 0.9, 1.1, 1.3, and 1.7 mm for groups S1, S2, S3, and S4, respectively. The hardness of untreated group S0 is about 364 HV.

Gradient microstructures were obtained after surface carburization treatment, and the microstructures of S1–S4 are displayed in **Figure 3**. It is clear that from surface to center, the size of carbides decreases and the shape changes from plates to spheres as observed in the SEM image. To further analyze the carbides, the EBSD and EDS mapping were used for characterization, and the results are shown in **Figure 4**. It is clear that the Cr- and Mo-rich carbides could be related to $M_{23}C_6$- and M_6C-type carbides, respectively.

As the hardness gradient is mainly caused by the distribution of carbides, the variations of carbide size with depth of groups S1–S4 are shown in **Figure 5**. The carbide size is represented by the equivalent circular diameter with equal area. The sizes of all the carbides inside the SEM image at a specific depth were calculated as shown by the hollow circles in Figure 5. It is clear that as the effective case depth increases, the size of carbides near the surface becomes larger. The carburizing potential was the same for all four processes, with the only difference being the carburizing time. Additionally, the process temperature was also consistent across all samples and should have a uniform impact on the formation and size of the carbides. Therefore, the variation in carbide size observed might primarily due to the different carburizing times.

For group S1, the average carbide size varies significantly with depth, while there is little variation in the maximum carbide size within the depth of 0–800 μm. This is because the microstructure contains two types of carbides: large-sized $M_{23}C_6$ and small-sized M_6C, and as the depth increases, the number of $M_{23}C_6$ decreases, while the number of M_6C does not change much, resulting in a decrease in average size and little change in the maximum size. For groups S2, S3, and S4, the maximum size of carbides varies significantly with depth. This might be explained by the fact that the carbides near the sample surface begin to come into contact with each other.

In addition, the variations of phase content with depth for S1–S4 are shown in **Figure 6**. It could be seen that only the trend of carbides content is similar to that of the hardness. The content of residual austenite shows significant changes around the

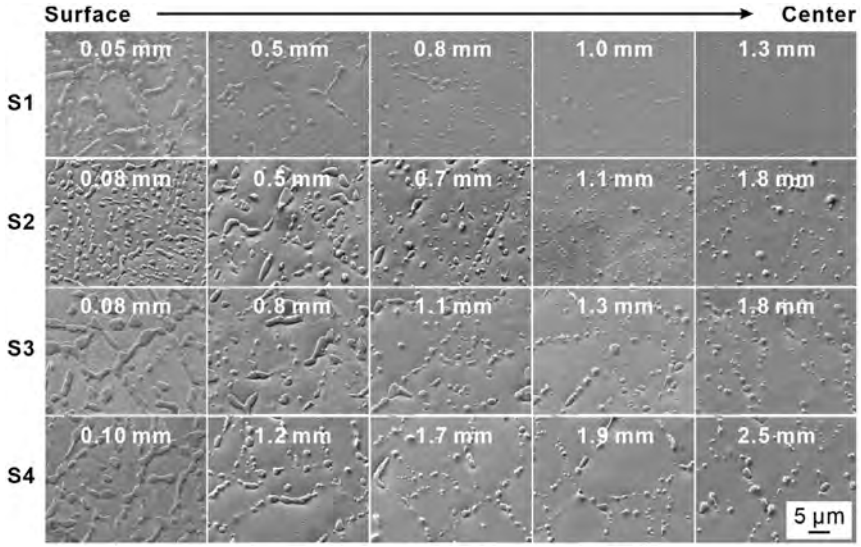

Figure 3. The SEM images of carburized steels across S1–S4 groups. The distance from the sample surface is marked on the SEM images. All images share the same scale.

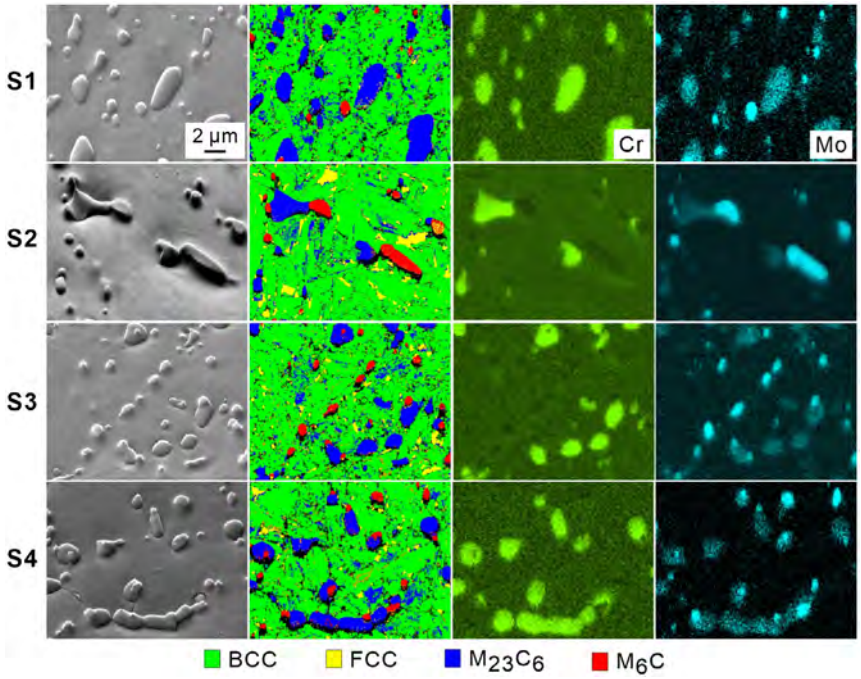

Figure 4. Micrographs of SEM, EBSD, and EDS results showing typical microstructures of the carburized steels across S1–S4 groups. All images share the same scale.

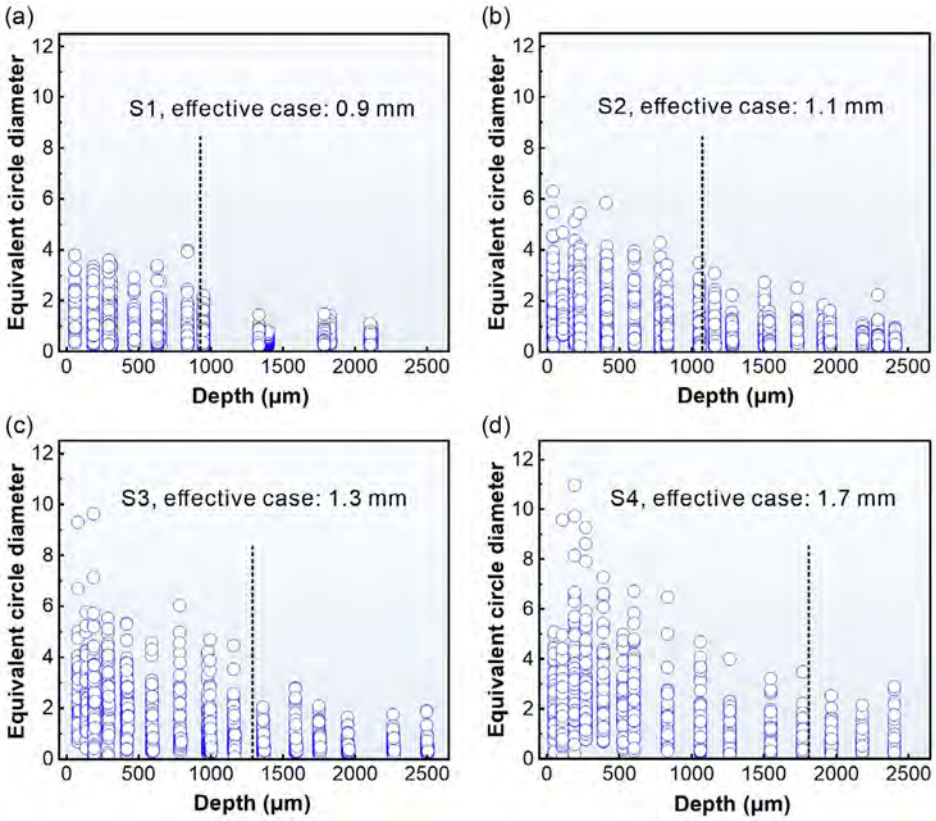

Figure 5. The variation in carbide size with depth of carburized steels for a) S1, b) S2, c) S3, and d) S4.

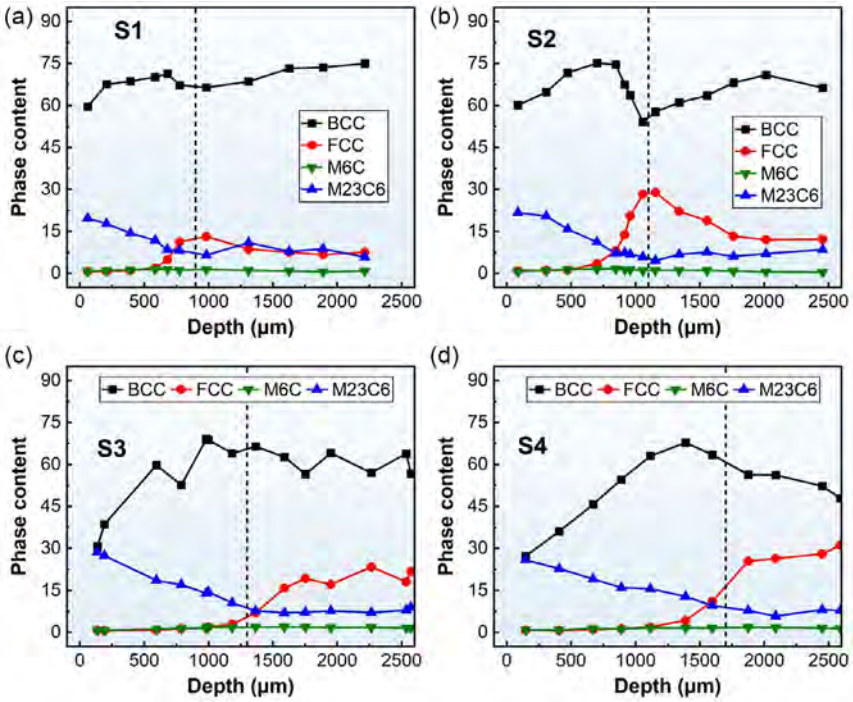

Figure 6. The variation in phases content with depth of carburized steels for a) S1, b) S2, c) S3, and d) S4.

effective case depth. However, taking S2 as an example, this change could not be clearly associated with the hardness.

The residual stress distribution of groups S1–S4 is shown in **Figure 7**. The maximum value of the residual compressive stress is on the surface and then the residual compressive stress gradually decreases for all groups. It was reported that the carbon content of the surface layer of the carburized samples is higher than that of the core, leading to the formation of a surface-hardened layer with compressive residual stress.[3,9,24,25] In this study, the maximum compressive residual stress for groups S1, S2, S3, and S4 was −864, −658, −964, and −727 MPa, respectively.

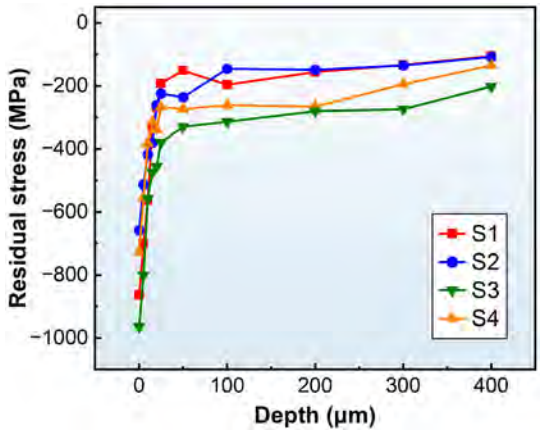

Figure 7. The variation in residual stress with depth of carburized steels for groups S1–S4.

3.2. Fatigue Strength

The stress–life diagram at room temperature is shown in **Figure 8**a, and the dependence of fatigue strength on effective case depth can be seen in Figure 8b. The fatigue strengths were obtained by the staircase method and the error bars were indicated by the stress steps. The detailed staircase plots are displayed in Figure 8c–f. It could be seen that the fatigue strength of the carburized steels increases considerably compared with the untreated material. Furthermore, the group S3 exhibits the optimal fatigue strength among the five groups of steels. The fatigue strengths are 708 ± 15, 1020 ± 20, 1025 ± 25, 1058 ± 25, and 958 ± 25 MPa for S0, S1, S2, S3, and S4, respectively. The improvement up to 49% of fatigue strength is achieved with the modified carburizing employed in the present study.

As the effective case depth increases from 1.3 to 1.7 mm, the fatigue strength shows a decreasing trend. Xiao et al.[12] summarized the changes in fatigue strength with relative case depth t/D (ratio of effective case depth and diameter of sample) of several case-hardened steels, indicating that fatigue strength of the carburized steels generally increased with an increase in t/D up to about 0.17; however, with further increasing t/D, there was a decreasing tendency of the fatigue strength. In the present study, the optimal fatigue strength of the carburized steel appeared at t/D of 0.26. However, the effective case depth alone could not fully represent carburized material because there are many factors affecting the fatigue properties of carburized steels, mainly including the distribution of residual compressive stress and carbides.[13,14] Therefore, other significant factors are needed to be considered.

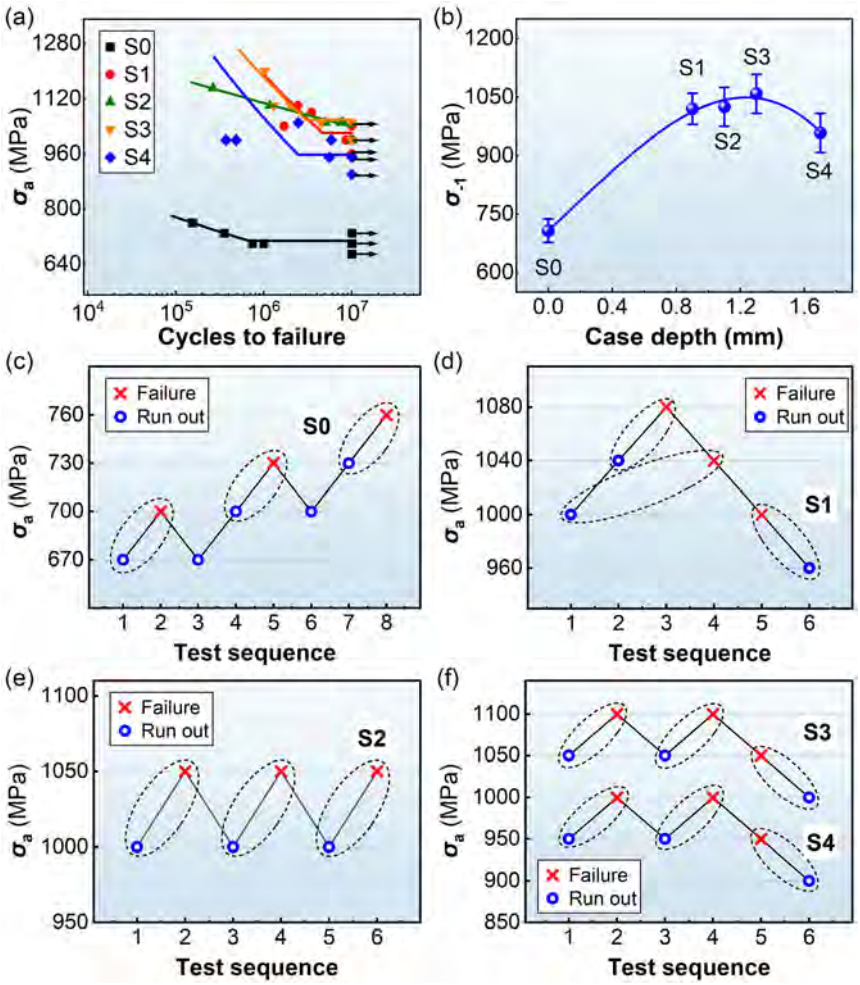

Figure 8. Fatigue performance of the 14Cr14Co13Mo5 steels for S0, S1, S2, S3, and S4. a) *S–N* curves. b) Relationship between the fatigue strength and effective case depth. Staircase plots of c) S0, d) S1, e) S2, and f) S3 and S4.

3.3. Fatigue Fracture

The typical fracture morphology of the group S0 is shown in **Figure 9**. Fatigue cracking originates on the surface of the sample due to cyclic sliding deformation, through the well-known mechanism of intrusions and extrusions.[26–28] This mechanism operates in the group S0 regardless of stress level. After crack initiation, the crack grew radially into the interior of the sample.

In the carburized groups S1–S4, the crack initiation occurred in the subsurface of the sample and within the carburized case, as shown in **Figure 10**. A close examination reveals that there exists a fish-eye-like pattern and its diameter is ≈100 μm. The

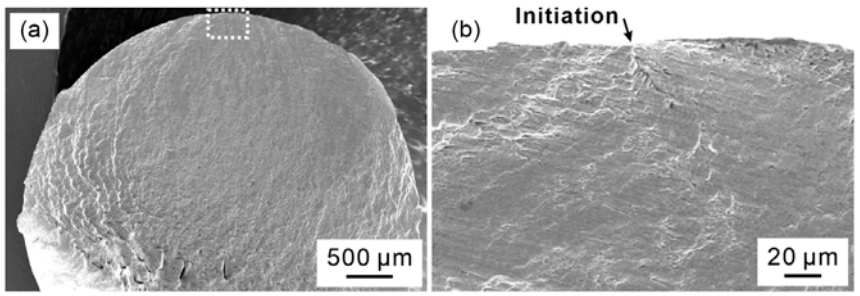

Figure 9. SEM micrographs of fatigue fracture of the untreated steel S0: a) low-magnification and b) high-magnification image on the fatigue crack initiation site.

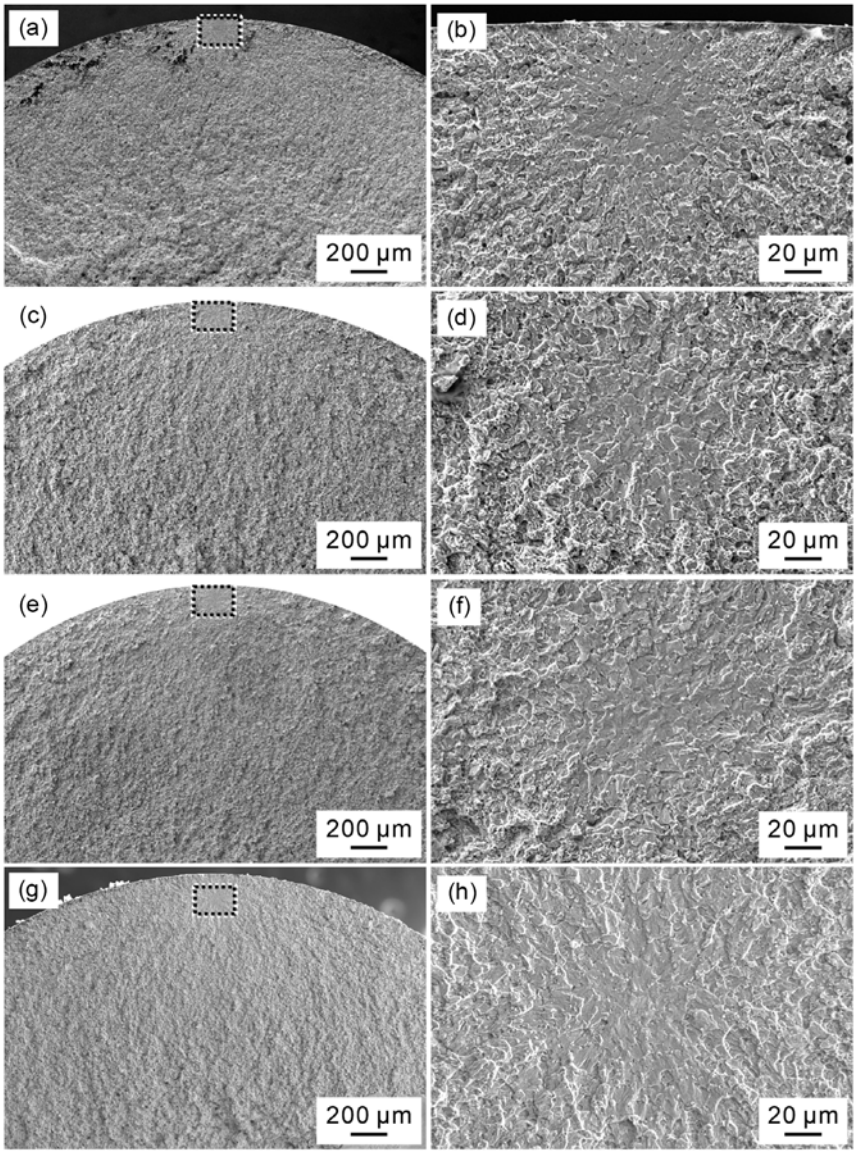

Figure 10. SEM micrographs of fatigue fracture of the carburized steels: a,b) S1; c,d) S2; e,f) S3; and g,h) S4.

depth of the crack initiation site will affect the effective external stress, as the stress distribution under rotational bending loading is gradient, accordingly the stress decreases from the surface to the core.

The definition of the depth of the crack initiation site is shown in **Figure 11**a and the statistical results are displayed in Figure 11b. It can be seen that the data range between 40 and 160 μm for the groups S2–S4 and 40–80 μm for the group S1. The difference may be mainly caused by the residual stress gradients. As the residual compressive stress increases, the depth of the crack initiation site becomes deeper. In addition, within these depth ranges, the microstructure, including carbide, plays a secondary role, which leads to differences in the depth of crack initiation site between different samples.

3.4. Carbides in Fatigue Crack Initiation Site

The EDS analysis of the fatigue crack initiation site reveals that two cases exist, as shown in **Figure 12**: case A—only Cr-rich carbides are detected; case B—both Cr- and Mo-rich carbides are detected. From a material perspective, there is only case A in group S1, while both case A and case B exist in groups S2–S4. For all carburized steel (groups S1–S4), there is either a large Cr-rich carbide or a large cluster of Cr- and Mo-rich carbides in the center of the fatigue crack initiation site.

The element distributions of case B are further analyzed, as shown in **Figure 13**. In line analysis, the counts of *C*, *V*, and *W* elements are relatively small, so they are not displayed. The positions of line and point analysis are marked in Figure 13a, and the results are drawn in Figure 13b,c and listed

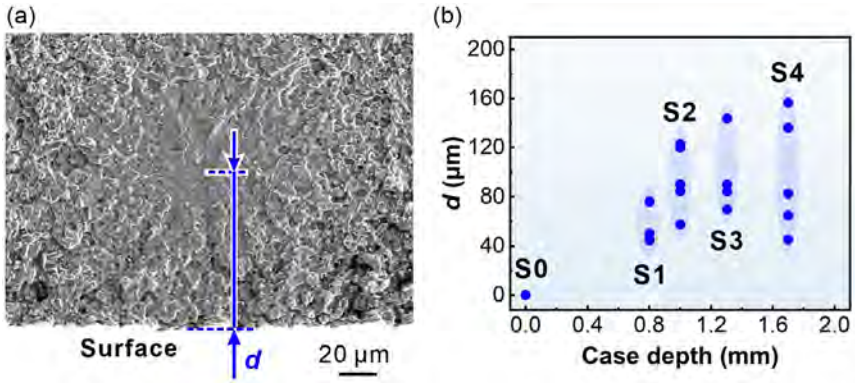

Figure 11. Typical fatigue crack initiation site of the carburized steels: a) SEM and b) the relationship between *d* (depth of the initiation site) and the effective case depth.

in **Table 2**, respectively. It was verified that the white carbides are Mo-rich, and the gray carbides are Cr-rich. Both Cr- and Mo-rich carbides in the fatigue crack initiation site show some smooth facets, which are the characteristics of cleavage fracture. Furthermore, a particularly persuasive feature of cleavage fractures is the river-like pattern evident in Mo-rich carbides, as depicted in Figure 13d.

The content of Cr element (atomic percentage) in Cr-rich carbides remains stable at 22%, and the content of Mo element (atomic percentage) in Mo-rich carbides remains stable at 18%. The Cr content in the matrix is close to that in the Mo-rich carbides, while the Mo content in the matrix is much smaller than that in the two carbides.

The cracking mechanisms of carburized and untreated steels are significantly different. For the S0 steel, it is well known that the fatigue cracks would initiate due to the irreversible slip of dislocation causing the accumulation of plastic deformation in large grains at surface for steel without inclusions.[29] In addition, because of the lack of carburizing, there is no residual compressive stress in the sample surface. Furthermore, the maximum stress during rotational bending loading occurs on the surface of the sample. The above factors may contribute to the fatigue failure mechanism of the group S0.

As for the carburized steel (groups S1–S4), the carbides are considered one of the key factors in the fatigue failure mechanism. Du et al.[30] showed that under monotonic loading, large M_2C and MC carbides will crack at a stress of around 700 MPa. The microhardness of M_2C and MC is in the range of 1500–2000 HV, while the microhardness of $M_{23}C_6$ is in the range of 1300–1650 HV.[31] According to the general relationship between strength and hardness of ceramics, the higher the hardness is, the greater is the strength.[32] Therefore, the critical stress required for the cracking of $M_{23}C_6$ and M_6C carbides should be slightly lower than 700 MPa. In addition, the complex shape of carbide clusters may further reduce the nominal stress required for them to undergo cleavage fracture. The fracture of carbide clusters was observed in sample that had not undergone fatigue test, as shown in **Figure 14**. It may have cracked during the sanding process.

However, even if the loading stress is larger than the stress needed for carbide cracking, the sample might not fail when the SIF at the crack tip is less than the crack propagation threshold of the matrix. Only when the loading stress further increases, the crack would be able to propagate into the matrix. Nevertheless, due to the finite conditional life of fatigue test, when the test is manually stopped, the SIF at the crack tip might not yet have reached the K_{IC} required for unstable fracture, and the sample might still not have failed. Finally, as the loading stress continues to increase, the accelerated crack propagation could result in the final failure within the finite conditional life. In summary, it is inferred that the fatigue failure is due to the local cleavage fracture of carbides, leading to fatigue crack initiation within a few cycles at the beginning of the fatigue test, and the crack propagation may dominate the fatigue life.

3.5. Fast Evaluation of Fatigue Strength

Based on the assumption that the fatigue failure is caused by carbide cracking and subsequent fatigue crack propagation, the factors affecting fatigue strength should include the carbide size and position, residual stress, and the fatigue crack resistance of the matrix. Once the material processing is determined, these factors are also determined, so as long as the relationship between these factors and fatigue performance is established, the fatigue performance can be quickly evaluated.

Generally, there are two ways to obtain the size of carbides: from metallographic photographs and from fatigue fractographies as shown in **Figure 15**a–d. It can be seen that the carbide sizes counted from the fatigue fracture surface are much larger than that in the metallographic images, despite many metallographic photos have been collected. This is because the number of large-sized carbides in the sample may be limited, and the metallographic images can only cover a small part of the gauge section of the sample, so the probability of capturing the largest sized carbides is very low. Furthermore, the cross section is usually not in the plane of the largest diameter of the carbide being examined. While for fatigue fracture, the fatigue crack initiation usually occurs at the carbide with the largest size.[33] This also suggests that evaluating fatigue performance based solely on carbide sizes obtained from metallographic photographs may lead to an overestimation.

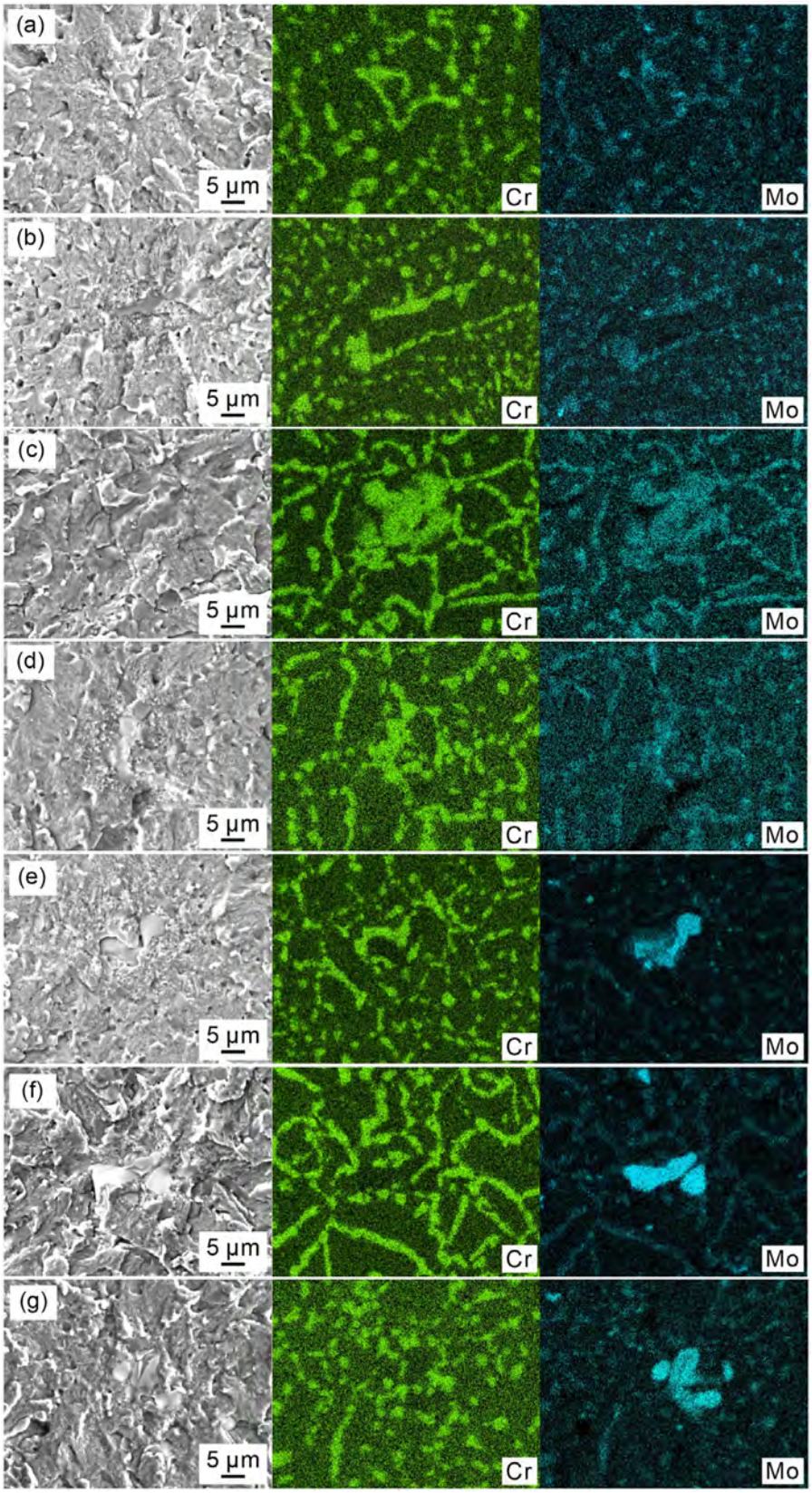

Figure 12. SEM and EDS results of fatigue crack initiation site of carburized steels. Cr-rich carbides: a) S1, b) S2, c) S3, and d) S4; Mo-rich carbides: e) S2, f) S3, and g) S4.

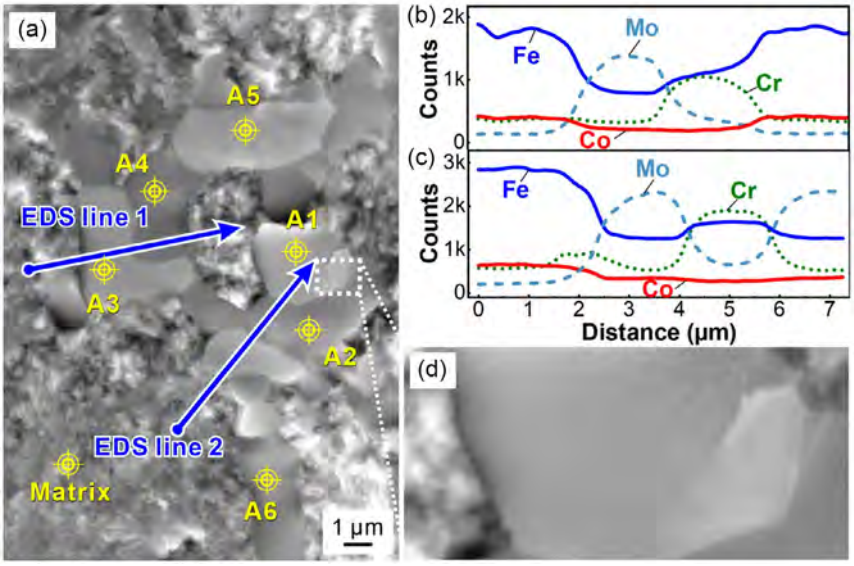

Figure 13. EDS analysis of the carbides in fatigue crack initiation site: a) SEM image of sample from S3; b) EDS line 1; c) EDS line 2; and d) high magnification of mark in (a).

Table 2. Chemical compositions of selected carbides analyzed by SEM–EDS (at%).

Position	Type	Mo	Cr	Co	Fe
A1	Mo-rich	18.3	5.8	4.3	20.8
A2	Cr-rich	5.5	21.4	3.0	25.7
A3	Mo-rich	18.5	6.5	4.7	22.7
A4	Cr-rich	3.9	22.1	3.9	30.8
A5	Mo-rich	18.7	6.0	4.7	22.2
A6	Cr-rich	3.7	22.1	3.0	26.7
Matrix	–	1.1	6.9	11.2	56.7

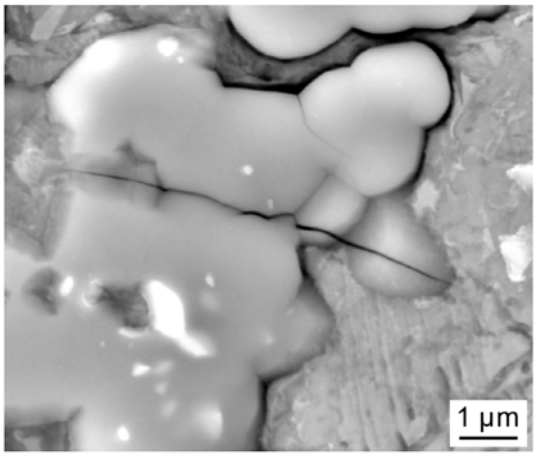

Figure 14. The fracture of carbide clusters with complex shape in the sample of carburized steel without fatigue test.

In order to illustrate what determines the fatigue strength, Figure 15e plots and shows the relationship between the SIF of carbides and fatigue life. The SIF of inner defects is recommended by Murakami[23] to be calculated by

$$K_{\mathrm{cbd}} = 0.5\,\sigma_{\max}\sqrt{\pi\sqrt{\mathrm{area}}} \tag{1}$$

where K_{cbd} is the SIF of carbide, area is the projection area of the carbide along the loading direction, and $\sigma_{\max}$ is the maximum local stress. Additionally, considering the carbide position and the residual stress, the local stress could be calculated by

$$\sigma_{\max} = \sigma_{\mathrm{a}}(1 - d/r) + \sigma_{\mathrm{RS}} \tag{2}$$

where d is the depth of the initiation site, r is the radius of the sample, and σ_{RS} is the residual stress.

Furthermore, it is found that the relationship between the fatigue life and the SIF of carbides, as plotted in Figure 15e, could be described by

$$K_{\mathrm{cbd}} = K_0 + C(N_{\mathrm{f}})^{\mathrm{m}} \tag{3}$$

where the K_0, C, and m are material-related constants. The equations are as follows:

$$K_{\mathrm{cbd}} = 1.9 + 38837(N_{\mathrm{f}})^{-0.8} \tag{4}$$

$$K_{\mathrm{cbd}} = 2.2 + 21143(N_{\mathrm{f}})^{-0.8} \tag{5}$$

$$K_{\mathrm{cbd}} = 1.9 + 41127(N_{\mathrm{f}})^{-0.8} \tag{6}$$

$$K_{\mathrm{cbd}} = 2.0 + 15177(N_{\mathrm{f}})^{-0.8} \tag{7}$$

It is noted that $b = -0.8$ is suitable for all four series of samples. It may be related to the composition of the material

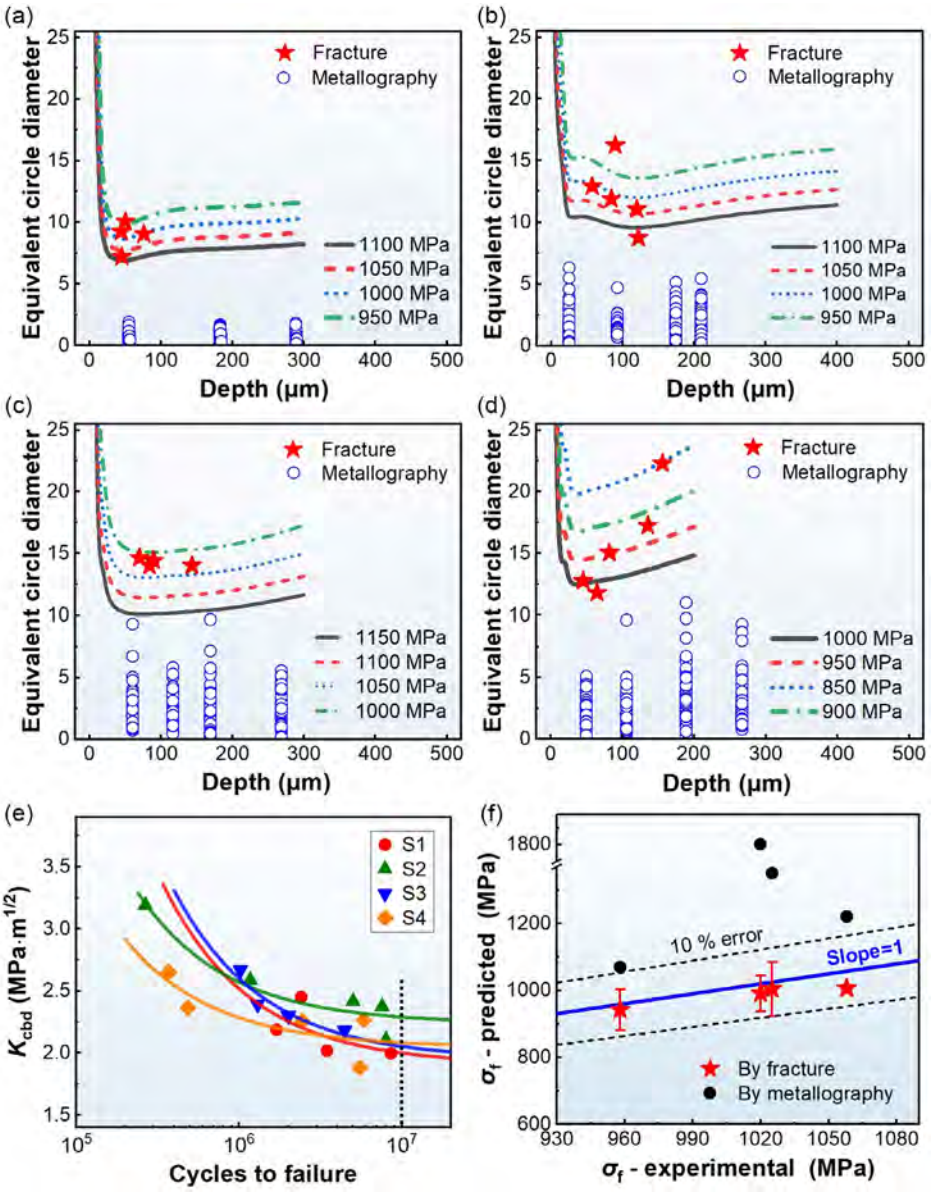

Figure 15. Fast evaluation of fatigue strength of the carburized steels. The carbide size of a) S1, b) S2, c) S3, and d) S4; e) the relationship between effective SIF and fatigue life; f) comparation of predicted fatigue strength using carbide size obtained by fracture and metallography.

matrix at the subsurface of samples, which has not changed significantly. This type of data in Figure 15e is quite common in the literature.[19,34–39] Therefore, it is reliable to evaluate the fatigue strength through Equation (3).

For a certain sample, the carbide size is usually determined and remains unchanged when the applied loading stress alters. By reducing the stress amplitude σ_a, the corresponding K_{cbd} also decreases according to Equation (3); thus, the fatigue life should increase accordingly. When the fatigue life reaches 10^7 cycles, the corresponding stress amplitude would be the predicted fatigue strength. The critical K_{cbd} at 10^7 cycles (K_C) could be calculated as 2.0, 2.3, 2.1, and 2.1 MPa m$^{-1/2}$ for groups S1, S2, S3, and S4, respectively. The predicted fatigue strength could be calculated by:

$$\sigma_a = \left(\frac{K_C}{0.5\sqrt{\pi\sqrt{area}}} - \sigma_{RS}\right)\frac{1}{1-d/r} \quad (8)$$

Based on the data from each fatigue fracture, a fatigue strength can be predicted by Equation (8). With at least four valid fatigue fractures for each group of carburized steel, the final predicted fatigue strength is determined as the average of these predicted fatigue strengths for each group. The error in this determination is represented by the standard deviation of these predicted fatigue strengths for each group. The comparison of the predicted fatigue strength using carbide size obtained by fracture and metallography is displayed in Figure 15f. It can be seen that the predicted fatigue strength based on fractographies is

within 10% error and is conservative. This might be attributed to the fact that the data used for establishing the relationships (Equation (4)–(7)) were all from the broken samples, as run-out samples, which could potentially be used in the staircase method, were not available. On the contrary, the predicted fatigue strength based on metallography is substantially overestimated because the probability to obtain the maximum size of carbides through metallographic method is extremely low.

The critical carbide size under fixed stress amplitude can also be calculated. Due to the gradient distribution of residual stress and the external stress, the critical carbide size varies with depth, as described by lines in Figure 15a–d. It is clear that a small carbide size and high residual compressive stress are beneficial to improve the fatigue performance of the present steel. These lines in Figure 15a–d also indicate that the subsurface position is the most dangerous for fatigue crack initiation and the change of the external loading stress has limited influence on the depth of potential crack initiation location.

Based on the analysis above, the fatigue failures of carburized steels are usually caused by local cracking of large-sized carbides. The maximum size of carbide can be revealed through fatigue tests at relatively higher stress amplitudes, which usually has much lower fatigue life and consumes shorter testing time. By using these short-life data, the relationship between stress amplitude and fatigue life can be established, thereby predicting the long-life fatigue strength.

It is important to note that our method for assessing fatigue strength utilizes fractured samples, which typically exhibit shorter lifetimes compared to samples tested using methods such as the staircase (up-and-down) method. In our study, the total testing time for all the failure samples analyzed was 6.2×10^7 cycles, whereas the total testing time for samples tested using the staircase method was 17.4×10^7 cycles. This comparison demonstrates that our method offers a significant time savings of ≈65%. The reduction in testing time is a crucial advantage of our method, as it allows for more efficient use of resources and can expedite the process of material evaluation and development. Furthermore, our method also reduces the number of samples required from 24 to 18, which further enhances its practicality and cost-effectiveness.

3.6. Factors Affecting Fatigue Strength

There are several factors that can affect the fatigue performance of carburized steel according to Equation (8). The material-related factors that can be quantified are the carbide size, the residual compressive stress, and the crack propagation resistance of matrix (K_C).

The group S2 has the highest K_C and the lowest microhardness simultaneously. This may be attributed to that the steels with lower microhardness generally have better plasticity and toughness, resulting in higher resistance to fatigue crack propagation. However, the difference of K_C for four group steels is not significant. This may be because the carburizing carbon potential and temperature of the steels from four groups are the same, resulting in similar mechanical properties of martensitic matrix.

As for the carbide size, it refers to a single carbide or a carbide cluster, rather than the carbide volume fraction. A large residual compressive stress requires long carburization time, which can lead to a high carbide volume fraction. However, when the carbide size is uniformly distributed, a large carbide volume fraction and small carbide size can coexist. The carbide should be detrimental to fatigue performance, as it would exhibit cleavage fracture when the crack tip approaches, leading to a sudden increase in crack length. The average carbide volume fractions in fatigue initiation sites are 8%, 16%, 21%, and 15% for S1, S2, S3, and S4, respectively. Although S3 has the highest carbide volume fraction in fatigue initiation site, its carbide sizes are uniform (as shown in Figure 15c) and its residual compressive stress is the maximum. This indicates that the fine and uniform carbides, as well as high residual compressive stress, are the most important factors beneficial to the fatigue performance.

4. Conclusions

In the present study, rotary bending fatigue tests were performed using samples with four different effective case depths of a 14Cr14Co13Mo5 gear steel. The fatigue strength was evaluated and fracture mechanisms were discussed on the basis of observation of crack initiation and fracture surface analysis. A fast evaluation method for fatigue strength was proposed. The main conclusions are as follows: 1) The fatigue strength of the carburized steel increased considerably compared with the untreated steel. Compared with the fatigue strength of 708 MPa for noncarburized samples, the fatigue strength of the carburized samples in group S3 is as high as 1058 MPa. The relationship between the effective case depth and the fatigue strength is not monotonically increasing; 2) The fatigue failure mode of the steel changed from surface failure to internal failure after being carburized, and the internal failure mode is induced by carbide cluster cracking. A small carbide size and high residual compressive stress are beneficial to improve the fatigue performance of the present carburized steel; 3) It is possible to predict the fatigue strength at long conditional life through the data of the samples tested at high stress amplitude with short life. The error of the predicted fatigue strength is within 10% for the present material. Although the methodology can offer a degree of time efficiency in evaluating fatigue strength, its applicability is confined to scenarios where defects initiate cracking at a very early stage; and 4) The total testing time for all the failure samples employed by the present method was 6.17E7 cycles. This represents a significant time savings of ≈65% compared to the 17.4E7 cycles required by the staircase method. In addition, the number of required samples also decreases from 24 to 18 in the present study. The fatigue strength assessment method proposed in this study not only improves testing efficiency but also reduces costs. It is expected that this method will be validated in more material systems.

Acknowledgements

This work was financially supported by the National Science and Technology Major Project under grant no. J2019-VI-0019-0134; the National Natural Science Foundation of China (NSFC) under grant nos. 52321001, 52130002, and 52371123; and the IMR Innovation Fund under grant no. 2024-PY07.

Conflict of Interest

The authors declare no conflict of interest.

Author Contributions

Zikuan Xu: Conceptualization (lead); Data curation (lead); Formal analysis (lead); Investigation (supporting); Writing—original draft (lead). **Xuezhong Gu**: Investigation (equal). **Xiaolong Liu**: Investigation (supporting). **Weihao Chen**: Investigation (equal). **Bin Wang**: Methodology (lead); Resources (supporting); Supervision (lead). **Peng Zhang**: Supervision (supporting). **Maosheng Yang**: Resources (equal); **Hongxiao Chi**: Resources (equal). **Zhefeng Zhang**: Supervision (supporting); Writing—review and editing (lead).

Data Availability Statement

The data that support the findings of this study are available from the corresponding author upon reasonable request.

Keywords

carbides, carburizing, fatigue strength prediction, high-cycle fatigue, martensitic stainless steels

Received: August 31, 2024
Revised: November 7, 2024
Published online:

[1] G. Wang, X. Sang, Y. Zhang, M. Zhao, G. Xu, Z. Peng, *J. Mater. Res. Technol.* **2023**, *25*, 1649.
[2] S. W. Qin, L. X. Wang, L. Y. Di, C. H. Zhang, M. H. Zhao, *Eng. Failure Anal.* **2023**, *147*, 107161.
[3] S. W. Qin, C. H. Zhang, B. Zhang, H. Y. Ma, M. H. Zhao, *J. Mater. Res. Technol.* **2022**, *16*, 1136.
[4] Z. Liu, S. Wang, Y. Feng, X. Wang, Y. Peng, J. Gong, *Mater. Sci. Eng., A* **2022**, *850*, 143562.
[5] S. W. Thompson, V. Parthasarathi, K. O. Findley, *Mater. Sci. Eng., A* **2021**, *807*, 140812.
[6] S. Parareda, D. Casellas, A. Lara, A. Mateo, *Int. J. Fatigue* **2022**, *156*, 106643.
[7] S. Parareda, D. Casellas, M. Mares, A. Mateo, *Mater. Des.* **2023**, *231*, 112056.
[8] H. Wu, C. Sun, W. Xu, X. Chen, X. Wu, *Eng. Fract. Mech.* **2023**, *290*, 109482.
[9] O. Asi, A. Ç. Can, J. Pineault, M. Belassel, *Surf. Coat. Technol.* **2007**, *201*, 5979.
[10] K. Genel, *Surf. Coat. Technol.* **2005**, *194*, 91.
[11] K. Genel, M. Demirkol, *Int. J. Fatigue* **1999**, *21*, 207.
[12] N. Xiao, W. Hui, Y. Zhang, X. Zhao, Y. Chen, H. Dong, *J. Mater. Eng. Perform.* **2019**, *28*, 3413.
[13] O. Asi, A. Ç. Can, J. Pineault, M. Belassel, *Mater. Des.* **2009**, *30*, 1792.
[14] D. K. Matlock, K. A. Alogab, M. D. Richards, J. G. Speer, *Mater. Res.* **2005**, *8*, 453.
[15] V. Savaria, F. Bridier, P. Bocher, *Int. J. Fatigue* **2016**, *85*, 70.
[16] L. C. Yin, X. X. Ma, G. Z. Tang, Z. Y. Fu, S. X. Yang, T. J. Wang, L. Q. Wang, L. H. Li, *Surf. Coat. Technol.* **2019**, *358*, 654.
[17] Y. Tian, C. W. Song, B. Wang, Z. D. Wang, G. D. Wang, H. J. Wang, *Steel Res. Int.* **2022**, *93*, 2100849.
[18] Y. He, X. J. Zeng, L. Q. Li, N. Li, J. B. Niu, X. X. Ma, *Surf. Coat. Technol.* **2024**, *484*, 130868.
[19] J. Guo, A. Zhao, M. Yang, *Int. J. Fatigue* **2023**, *174*, 107587.
[20] S. Schmid, M. Hahn, S. Issler, M. Bacher-Hoechst, Y. Furuya, A. Mehner, H. Bomas, H. W. Zoch, *Int. J. Fatigue* **2014**, *60*, 90.
[21] C. R. Sohar, A. Betzwar-Kotas, C. Gierl, B. Weiss, H. Danninger, *Int. J. Fatigue* **2008**, *30*, 1137.
[22] Y. Xue, Y. Yan, W. Yu, M. Dong, J. Shi, M. Wang, *Int. J. Fatigue* **2023**, *167*, 107314.
[23] Y. Murakami, in *Metal Fatigue: Effects of Small Defects and Nonmetallic Inclusions*, Elsevier Science Ltd, Oxford **2002**.
[24] S. Farfan, C. Rubio-Gonzalez, T. Cervantes-Hernandez, G. Mesmacque, *Int. J. Fatigue* **2004**, *26*, 673.
[25] Z. N. Yang, Y. L. Ji, F. C. Zhang, M. Zhang, B. Nawaz, C. L. Zheng, *Mater. Sci. Eng., A* **2018**, *725*, 98.
[26] S. Suresh, in *Fatigue of Materials*, 2nd ed., Cambridge University Press, Cambridge, UK **1998**.
[27] L. Kunz, P. Lukáš, M. Svoboda, *Mater. Sci. Eng., A* **2006**, *424*, 97.
[28] J. Tian, W. Wang, H. Li, K. Yang, Z. Jiang, *Mater. Sci. Eng., A* **2021**, *805*, 140589.
[29] S. Lavenstein, Y. Gu, D. Madisetti, J. A. El-Awady, *Science* **2020**, *370*, eabb2690.
[30] N. Y. Du, H. H. Liu, Y. F. Cao, P. X. Fu, C. Sun, H. W. Liu, D. Z. Li, *Mater. Charact.* **2022**, *186*, 111822.
[31] Z. Q. Lv, F. Dong, Z. A. Zhou, G. F. Jin, S. H. Sun, W. T. Fu, *J. Alloys Compd.* **2014**, *607*, 207.
[32] P. Zhang, S. X. Li, Z. F. Zhang, *Mater. Sci. Eng., A* **2011**, *529*, 62.
[33] S. X. Li, *Int. Mater. Rev.* **2012**, *57*, 92.
[34] P. Wang, B. Wang, Y. Liu, P. Zhang, Y. K. Luan, D. Z. Li, Z. F. Zhang, *Scr. Mater.* **2022**, *206*, 114232.
[35] K. Shiozawa, L. Lu, S. Ishihara, *Fatigue Fract. Eng. Mater. Struct.* **2001**, *24*, 781.
[36] D. Spriestersbach, P. Grad, E. Kerscher, *Int. J. Fatigue* **2014**, *64*, 114.
[37] Y. Furuya, *Mater. Sci. Eng., A* **2019**, *743*, 445.
[38] W. Li, T. Sakai, Q. Li, L. T. Lu, P. Wang, *Mater. Sci. Eng., A* **2011**, *528*, 5044.
[39] X. L. Gui, G. H. Gao, B. F. An, R. D. K. Misra, B. Z. Bai, *Mater. Sci. Eng., A* **2021**, *803*, 140692.